


Article

Investigation of the Influence of Alloy Atomic Doping on the Properties of Cu-Sn Alloys Based on First Principles

Zongfan Wei ¹, Jiaying Chen ¹, Jingteng Xue ¹, Nan Qu ¹, Yong Liu ^{1,*}, Ling Sun ^{2,3}, Yuchen Xiao ^{2,3}, Baoan Wu ^{2,3}, Jingchuan Zhu ^{1,*}  and Huiyi Tang ^{2,3,*}

¹ School of Materials Science and Engineering, Harbin Institute of Technology, Harbin 150001, China

² Chongqing Materials Research Institute Co., Ltd., Chongqing 400707, China

³ National Engineering Research Center for Instrument Functional Materials, Chongqing 400707, China

* Correspondence: lyonghit@hit.edu.cn (Y.L.); fgms@hit.edu.cn (J.Z.); hytang320@163.com (H.T.)

Abstract: In order to design Cu-Sn alloys with excellent overall performance, the structural stability, mechanical properties, and electronic structure of X-doped Cu-Sn alloys were systematically calculated using first-principles calculations. The calculation results of the cohesive energy indicate that the Cu-Sn-X structures formed by X atoms (X = Ag, Ca, Cd, Mg, Ni, Zr) doping into Cu-Sn can stably exist. The Cu-Sn-Ni structure is the most stable, with a cohesive energy value of -3.84 eV. Doping of X atoms leads to a decrease in the bulk modulus, Poisson's ratio and B/G ratio. However, doping Ag and Ni atoms can improve the shear modulus, Young's modulus, and strain energy of the dislocation. The doping of Ni has the highest enhancement on shear modulus, Young's modulus, and strain energy of the dislocation, with respective values as follows: 63.085 GPa, 163.593 GPa, and 1.689 W/J·m⁻¹. The analysis of electronic structure results shows that the covalent bond between Cu and X is the reason for the performance differences in Cu-Sn-X structures.

Keywords: Cu-Sn alloy; first-principles calculations; cohesive energy; mechanical properties; electronic structure



Citation: Wei, Z.; Chen, J.; Xue, J.; Qu, N.; Liu, Y.; Sun, L.; Xiao, Y.; Wu, B.; Zhu, J.; Tang, H. Investigation of the Influence of Alloy Atomic Doping on the Properties of Cu-Sn Alloys Based on First Principles. *Metals* **2024**, *14*, 552. <https://doi.org/10.3390/met14050552>

Academic Editor: Alain Pasturel

Received: 19 March 2024

Revised: 24 April 2024

Accepted: 30 April 2024

Published: 7 May 2024



Copyright: © 2024 by the authors. Licensee MDPI, Basel, Switzerland. This article is an open access article distributed under the terms and conditions of the Creative Commons Attribution (CC BY) license (<https://creativecommons.org/licenses/by/4.0/>).

1. Introduction

Copper alloys find extensive application in various industries including electrical, construction, and aerospace, owing to their exceptional conductivity, thermal conductivity, and resistance to corrosion [1–4]. However, the relatively low mechanical strength of pure copper limits its application in high-performance scenarios. Hence, enhancing the mechanical properties of copper alloys through alloying techniques has emerged as a central focus in the field of material science research. The study conducted by Ma et al. [5] reveals that doping Sc in the Cu-Cr-Zr alloy, combined with a treatment of solid solution, rolling, and aging, results in the formation of nanoscale precipitates and subgrains within the matrix. As a result, the mechanical properties of the Cu-Cr-Zr alloy are significantly improved, while the electrical conductivity experiences negligible reduction. Liu et al. [6] discovered that the incorporation of Cr, Zr, Ti, and Mg into the Cu-Ni-Si alloy leads to grain refinement and the formation of a twinning structure. Li et al. [7] showed that the addition of Mg in the Cu-Cr-Zr alloy, through a two-step deep cold rolling and aging process, effectively improves both the electrical and mechanical properties of the alloy. Huang et al. [8] discovered that the incorporation of Fe into the Cu-Ti alloy results in increased dislocation density, tensile strength, and quantity of deformation bands after cold rolling. Furthermore, the addition of Fe enhances the stress relaxation resistance of the Cu-Ti alloy. Lei et al. [9] designed a Cu-9Ni-1.5Sn-0.8Si-0.1Al alloy and employed multiple-stage deformation and heat treatment processes. As a result, the precipitation of Ni₃X (where X represents Sn, Si, and Al) notably enhances the tensile strength of the alloy.

In recent years, the effective utilization of first-principles calculations has guided the design of alloy compositions and facilitated the prediction of their performance.

Yang et al. [10] investigated the effect of different Al contents on the elastic properties of Cu-Al alloy using first-principles calculations. At 0 K, with increasing the Al content, the mechanical stability, shear modulus, bulk modulus, and Young's modulus of the alloy all show a decreasing trend. The best wear resistance and erosion resistance of Cu-Al alloy are achieved when the aluminum content is between 15.625 at.% and 18.750 at.% (at.% refers to atomic percent). Yang et al. [11] examined the role of Ni in Cu-Al-Mn alloy through a combination of first-principles calculations and experiments, showing that Ni not only significantly improves the shape memory effect of the alloy but also suppresses the temperature-dependent martensitic stabilization. He et al. [12] investigated the corrosion interface and characteristics of the Cu-C alloy in liquid Ga at temperatures ranging from 100 °C to 180 °C. The application of first-principles calculations unveiled that the diffusion of Ga atoms induces the phase transformation of Cu and initiates the formation of the corrosion product CuGa_2 . Dong et al. [13] investigated the intergranular precipitation behavior of the G phase ($\text{Ni}_{16}\text{Ti}_6\text{Si}_7$) in a high-performance casting Cu-Ni-Al alloy. Moreover, the application of first-principles calculations demonstrated that substituting Zr for Ti in the G phase is favorable for its formation and reduces the lattice mismatch at the G phase/matrix interface. Hideaki Iwaoka et al. [14] performed first-principles calculations to determine the elastic properties of Cu-Zn binary metal compounds. Their findings revealed that the Young's modulus of polycrystalline CuZn_4 aggregates is nearly equivalent to that of Cu_5Zn_8 aggregates, indicating low elasticity.

Cu-Sn (bronze) alloys are significant engineering structural materials with valuable applications in various fields such as aerospace, marine, and electrical appliances [15,16]. In the electronics industry, it is commonly used for manufacturing electronic components, such as electronic devices and circuit boards. These alloys exhibit exceptional characteristics, such as wear resistance, corrosion resistance, thermal conductivity, and electrical conductivity, while also maintaining adequate strength and ductility. According to the Cu-Sn phase diagram [17], the solid solution limit of Sn in the Cu matrix is 15.8 wt.% (the term "wt.%" denotes the weight percent). Within this solid solubility limit, increasing the Sn content can enhance the strength but may lead to a compromise in electrical conductivity and ductility. Conversely, reducing the Sn content can maintain high electrical conductivity and good ductility, albeit with a potential reduction in strength. The Sn content ranging from 5 to 11 wt.% finds its primary application in various fields such as bearings, shaft sleeves, and turbines [18]. In previous studies on Cu-Sn alloys, $\text{Cu}_{30}\text{Sn}_2$ (Sn content of 11.08 wt.%) has demonstrated the highest Young's modulus and elastic anisotropy [19]. Therefore, based on the structure of $\text{Cu}_{30}\text{Sn}_2$, this study aims to explore the effects of replacing Sn atoms in copper alloys with atoms X ($X = \text{Ag}, \text{Ca}, \text{Cd}, \text{Mg}, \text{Ni}, \text{Zr}$) that exhibit higher electrical conductivity. The focus is to investigate the alterations in the properties of the Cu-Sn-X structure and elucidate the underlying factors contributing to these changes. The influence of six alloying atoms on the structural stability, mechanical properties, and electronic structure of Cu-Sn alloys is explored through first-principles calculations. This approach offers an efficient means of selecting alloying elements, thus reducing the time and cost related to trial-and-error experimentation. Additionally, it provides a theoretical foundation for the development of high-strength and highly conductive Cu-Sn alloys.

2. Calculation Method and Material Structure

In Cu-Sn alloys, Sn exists in the form of a solid solution. Thus, a supercell model with Cu as the solvent and Sn as the solute is constructed. The supercell model adopts a face-centered cubic crystal structure with a $2 \times 2 \times 2$ size, containing a total of 32 metal atoms. As shown in Figure 1a, Sn replaces one vertex copper atom and one face-centered copper atom, resulting in a supercell configuration with 30 Cu atoms and 2 Sn atoms. Figure 1b depicts the inclusion of X atoms ($X = \text{Ag}, \text{Ca}, \text{Cd}, \text{Mg}, \text{Ni}, \text{Zr}$) of the Cu-Sn model. Consequently, the models consist of 30 Cu atoms, 1 Sn atom, and 1 X atom (hereafter denoted as Cu-Sn for $\text{Cu}_{30}\text{Sn}_2$ and Cu-Sn-X for $\text{Cu}_{30}\text{Sn}_1\text{X}_1$).

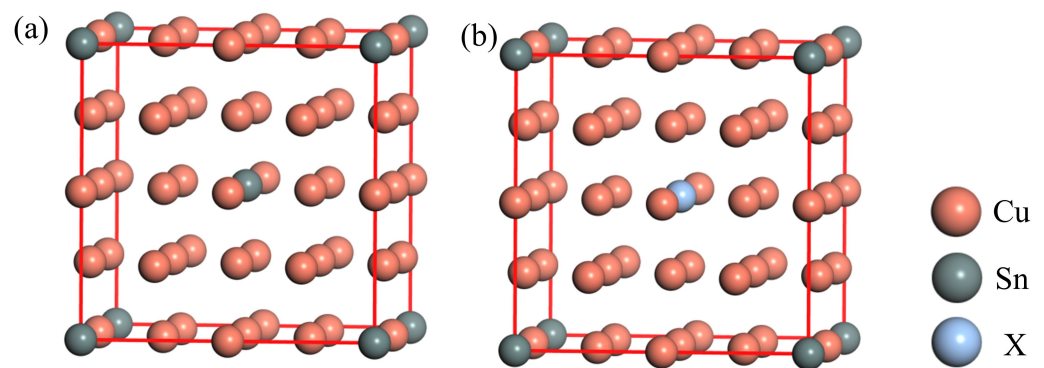


Figure 1. The structure of the Cu-Sn solid solution and the solid solution structure of Cu-Sn-X: (a) Cu-Sn solid solution structure, (b) Cu-Sn-X solid solution structure.

First-principles calculations were performed using the Cambridge Sequential Total Energy Package (CASTEP) software version 8.0 [20]. Periodic boundary conditions were employed, and the structural optimization was carried out using the Broyden–Fletcher–Goldfarb–Shanno (BFGS) method prior to each calculation. The calculation of exchange correlation functional is based on the high-precision Perdew–Burke–Ernzerhof (PBE) functional form selected from the Generalized Gradient Approximation (GGA) [21,22]. Ultrasoft pseudopotentials in reciprocal space representation were applied, with a cutoff energy set to 360 eV. A $4 \times 4 \times 4$ Monkhorst–Pack k-point grid was used. The total energy calculation employed the self-consistent field (SCF) method and was accelerated by the Pulay density mixing scheme for convergence [23]. The convergence criteria were set as follows: the total energy was lower than 5.0×10^{-6} eV/atom, the forces on each atom were less than 0.01 eV/atom, the displacement tolerance was lower than 5.0×10^{-5} nm, and the stress deviation was below 0.02 GPa.

3. Results and Discussion

3.1. Crystal Structure and Stability

The lattice constant is a fundamental parameter that reflects the crystal structure and internal composition, serving as the basis for studying material structure. Table 1 presents the optimized lattice constants and cohesive energy of Cu-Sn and Cu-Sn-X. To validate the accuracy of the computational results, the lattice constant of the pure copper model was compared with experimental data from other sources, revealing a difference of 0.414%. Generally, the disparity in lattice constants falls within 1%, indicating a well-chosen pseudopotential, as evidenced by the model, conditions, and parameters. The deviation between calculated and experimental values primarily arises due to the temperature-dependent nature of lattice parameters and the GGA process. Cohesive energy (E_{coh}) is defined as the energy needed to separate the crystal cell structure into individual atoms or the energy released when individual atoms combine to form a crystal cell [24]. In essence, a higher value of cohesive energy indicates the greater structural stability of the material. The calculation Equation (1) for the cohesive energy of Cu-Sn-X (where X = Ag, Ca, Cd, Mg, Ni, Zr) is shown below [25]:

$$E_{coh}(Cu_xSn_yX_z) = \frac{E_{tot}(Cu_xSn_yX_z) - xE_{atom}(Cu) - yE_{atom}(Sn) - zE_{atom}(X)}{x + y + z} \quad (1)$$

In the formula, E_{tot} denotes the total ground-state energy of the unit cell, which can be obtained by calculating the lattice constant of the model. $E_{atom}(Cu)$, $E_{atom}(Sn)$, $E_{atom}(X)$ denote the energies of the isolated Cu, Sn and X atoms, respectively; and x , y , and z are the number of Cu, Sn, and X atoms in the supercell, respectively. Figure 2 illustrates the cohesive energy of the Cu-Sn-X alloy. When X atoms are dissolved in the Cu-Sn alloy, they

can stably exist. Among them, the absolute value of the cohesive energy of Ni dissolved in the Cu-Sn alloy is the largest, and the resulting Cu-Sn-Ni structure is the most stable. The stability ranking for the cohesive of Cu-Sn-X structures is as follows: Cu-Sn-Ni > Cu-Sn-Zr > Cu-Sn-Ag > Cu-Sn-Mg > Cu-Sn-Ca > Cu-Sn-Cd.

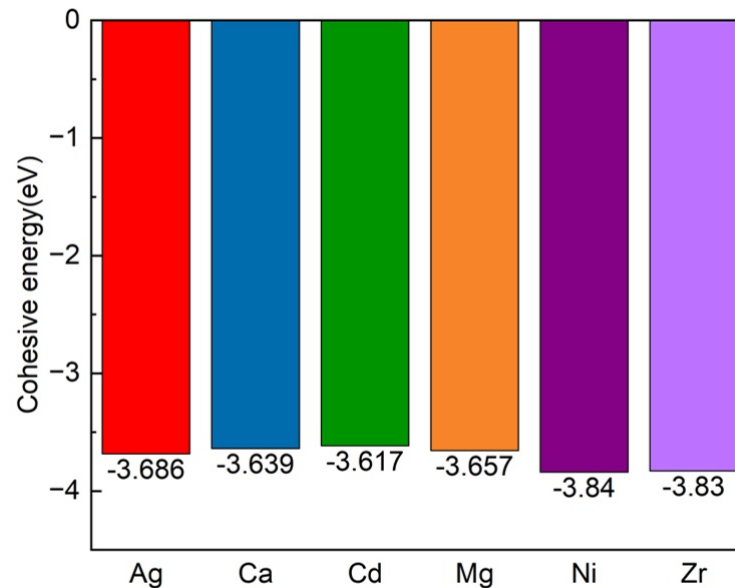


Figure 2. The cohesive energy of the Cu-Sn-X alloy.

Table 1. Optimized lattice parameters and cohesive energy for Cu-Sn and Cu-Sn-X alloys.

Structure	Source	a (Å)	α (deg)	E_{coh} (kJ/mol)
Cu	Exp at 25 °C [23]	3.615	90	-
	Present	3.630	90	-
	Error	0.414%	-	-
Cu-Sn	Present	7.229	90	-
Cu-Sn-Ag	Present	7.368	90	−3.686
Cu-Sn-Ca	Present	7.453	90	−3.639
Cu-Sn-Cd	Present	7.389	90	−3.617
Cu-Sn-Mg	Present	7.360	90	−3.657
Cu-Sn-Ni	Present	7.318	90	−3.840
Cu-Sn-Zr	Present	7.433	90	−3.830

3.2. Mechanical Properties

It is crucial to have a comprehensive understanding of the elastic constants of materials, because they encompass many key characteristics, such as solid stability, bonding properties, hardness, and processability. Elastic constants are quantities that establish a relationship between strain and stress, aiding in understanding the behavior of elastic materials. The analysis of mechanical properties in crystals is commonly performed using elastic constants. Within the Cauchy stress–strain method, the calculation of all independent elastic constants involves solving Hooke’s law, as depicted in Equation (2) [26]:

$$\sigma_i = \sum_{j=1}^{\sigma} C_{ij} \varepsilon_j, \quad (2)$$

where σ_i is the strain component for the i th component; $\sum_{j=1}^{\sigma}$ is the summation over j from 1 to σ , where σ is the total number of components; C_{ij} is the elasticity tensor between the i th and j th components; and ε_j is the strain component for the j th component.

For the cubic crystal system, there are three independent elastic constants, namely C_{11} , C_{12} , and C_{44} . The C_{11} coefficient signifies the resistance to unidirectional compression

(compression along the principal directions $\langle 100 \rangle$), while C_{44} characterizes the resistance to shear deformation across the (100) plane in the [110] direction. However, when the model derived from the disordered modeling of supercells undergoes geometric optimization, the number of independent elastic constants increases. This is due to the quasi-random distribution of solute atoms, which slightly breaks the crystal structure symmetry. The technique of symmetry-based projection (SBP) is employed to correct elastic tensors by projecting distorted elastic tensors onto their corresponding symmetric forms, aligning with the crystal symmetry of the material. This approach effectively eliminates symmetry-breaking components and facilitates the derivation of more precise and physically consistent elastic tensors. Therefore, in this study, we utilized the Symmetry-based Projection (SBP) technique to correct the elastic tensors of Cu-Sn-X [27,28]. To obtain the elastic constants of these quasi-random systems, we usually calculate the average values of the corresponding elastic parameters. This relationship is described by Equation (3) :

$$\begin{aligned}\overline{C_{11}} &= \frac{(C_{11} + C_{22} + C_{33})}{3} \\ \overline{C_{12}} &= \frac{(C_{12} + C_{13} + C_{23})}{3} \\ \overline{C_{44}} &= \frac{(C_{44} + C_{55} + C_{66})}{3}\end{aligned}\quad (3)$$

Average values of the relevant elastic parameters calculated for Cu-Sn and Cu-Sn-X (X = Ag, Ca, Cd, Mg, Ni, Zr) are shown in Table 2.

Table 2. Calculated values of elastic constants for Cu-Sn and Cu-Sn-X (X = Ag, Ca, Cd, Mg, Ni, Zr).

Structure	C_{11}	C_{22}	C_{33}	$\overline{C_{11}}$	C_{12}	C_{13}	C_{23}	$\overline{C_{12}}$	C_{44}	C_{55}	C_{66}	$\overline{C_{44}}$
Cu-Sn	208.336	207.863	208.137	208.137	178.681	178.849	178.605	178.711	88.438	88.432	88.445	88.438
Cu-Sn-Ag	187.246	187.085	187.057	187.130	104.073	104.070	104.267	104.137	77.932	78.289	78.278	78.166
Cu-Sn-Ca	142.597	142.598	143.467	142.887	111.261	108.654	108.668	109.528	67.180	67.143	65.625	66.650
Cu-Sn-Cd	143.442	143.451	130.855	139.250	122.416	118.995	119.046	120.152	77.720	77.740	77.246	77.569
Cu-Sn-Mg	136.668	136.538	136.388	136.531	111.485	117.329	117.264	115.359	77.041	77.041	80.190	78.091
Cu-Sn-Ni	184.447	184.461	185.989	184.966	110.125	107.830	107.844	108.560	87.363	87.363	90.339	88.355
Cu-Sn-Zr	160.133	160.0815	158.517	159.577	114.948	115.125	115.135	115.069	72.350	72.351	70.343	71.681

The stability criteria for different crystal structures are not the same. The elastic constants C_{11} , C_{12} , and C_{13} , as utilized in the subsequent text, all pertain to the average values that have been corrected using SBP technology. For the cubic crystal system, the criterion formula based on the Born stability rule is given by Equation (4):

$$\begin{aligned}C_{11} - |C_{12}| &> 0 \\ C_{11} + 2C_{12} &> 0 \\ C_{11} &> 0 \\ C_{44} &> 0\end{aligned}\quad (4)$$

Based on the calculated results of the elastic constants in Table 2, it can be observed that when X (X = Ag, Ca, Cd, Mg, Ni, Zr) atoms are doped into the Cu-Sn alloy, the crystal structure still maintains mechanical stability. As shown in Equation (5) [24], the obtained

three independent elastic constants can be further used to calculate the bulk modulus and shear modulus through the Voigt–Reuss (V-R) method.

$$\begin{aligned} B_V &= B_R = \frac{(C_{11} + 2C_{12})}{3} \\ G_V &= \frac{(C_{11} - C_{12} + 3C_{44})}{5} \\ G_R &= \frac{5(C_{11} - C_{12})C_{44}}{4C_{44} + 3(C_{11} - C_{12})} \end{aligned} \quad (5)$$

Using the Hill approximation, the bulk modulus (B) and shear modulus (G) can be further calculated [24]. The calculation Equation (6) is as follows:

$$\begin{aligned} B &= \frac{B_V + B_R}{2} \\ G &= \frac{G_V + G_R}{2} \end{aligned} \quad (6)$$

Utilize the bulk modulus and shear modulus for recycling purposes. As shown in Equation (7) [29], solve for the Young's modulus (E) and Poisson's ratio (ν) as follows:

$$\begin{aligned} E &= \frac{9BG}{3B + G} \\ \nu &= \frac{3B - 2G}{6B + 2G} \end{aligned} \quad (7)$$

The elastic modulus is a crucial indicator for characterizing the mechanical properties of materials, which encompasses the bulk modulus, shear modulus, and Young's modulus. Specifically, the bulk modulus is commonly employed to gauge a material's capacity to withstand compressive deformation under stress. Generally, a larger value of bulk modulus indicates a stronger resistance to compressive deformation, making the material more difficult to compress. As shown in Figure 3a, when no atoms are doped, the bulk modulus of the Cu-Sn alloy is 188.518 GPa. Compared to the Cu-Sn alloy, the structures formed after doping X (X = Ag, Ca, Cd, Mg, Ni, Zr) atoms all lead to a decrease in the bulk modulus. Among them, the largest decrease is observed when Ca atoms are doped, with a value of 120.637 GPa.

The shear modulus reflects a material's resistance to shear strain under shear stress. A larger shear modulus indicates a stronger resistance to shear strain, indicating greater rigidity of the material. As shown in Figure 3b, when Ag, Ni, and Zr atoms are doped into the Cu-Sn alloy, the shear modulus increases. On the other hand, doping of Ca, Cd, and Mg into the Cu-Sn alloy results in varying degrees of decrease in the shear modulus. The shear modulus increases slightly when Zr atoms are doped, while the doping of Ag and Ni atoms leads to a significant increase.

Within the elastic limit, the ratio of stress to strain is known as the Young's modulus, which reflects the material's stiffness. As shown in Figure 3c, when no alloy atoms are doped, the value of Young's modulus for the Cu-Sn alloy is 122.976 GPa. The doping of Ag and Ni atoms causes an increase in the Young's modulus, while the doping of Ca, Cd, Mg, and Zr atoms causes a decrease in the Young's modulus. After Ni doping, the maximum value of Young's modulus is 163.593 GPa, while the minimum value of Young's modulus during Cd doping is 96.16 GPa.

When a material is subjected to tensile or compressive forces, the absolute value of the ratio between transverse and axial positive strains is known as the Poisson's ratio, which typically ranges from -1 to 0.5 . A larger Poisson's ratio indicates better plasticity of the material, with values above 0.26 indicating plastic behavior. As illustrated in Figure 3d, the Cu-Sn and Cu-Sn-X structures both maintain plasticity. However, doping of X (X = Ag, Ca, Cd, Mg, Ni, Zr) atoms results in a decrease in the Poisson's ratio. Among them, the

doping of Ca, Cd, Mg, and Zr atoms causes a relatively small decrease, while the doping of Ag and Ni atoms leads to a significant decrease in the Poisson's ratio. The ratio of the bulk modulus to shear modulus B/G can be used to evaluate the plasticity and brittleness of a material. The criterion value is 1.75, where a B/G ratio greater than 1.75 indicates ductility, with larger values indicating better plasticity, while values below the criterion point to brittleness. As shown in Figure 3e, the trends of the Poisson's ratio and B/G ratio in the structures formed by X (X = Ag, Ca, Cd, Mg, Ni, Zr) atom doping are consistent.

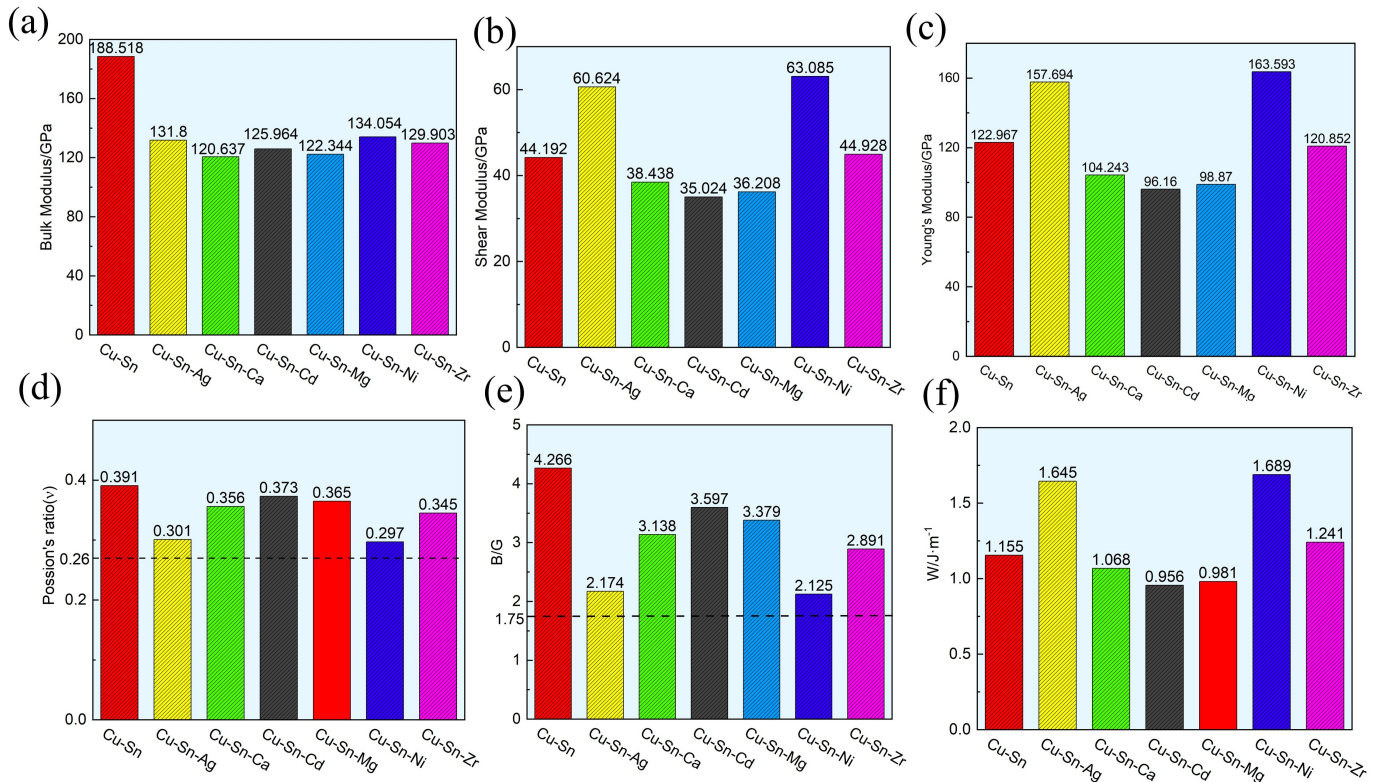


Figure 3. Cu-Sn alloy and Cu-Sn-X alloy mechanical properties: (a) Bulk modulus, (b) Shear modulus, (c) Young's modulus, (d) Poisson's ratio, (e) B/G ratio, (f) Dislocation strain energy.

Lattice distortion arises when X is solidly dissolved into the Cu-Sn structure, leading to an elastic stress field that raises the crystal energy. This crystal energy is defined as the strain energy of the dislocation [26],

$$W \approx Gb^2 \quad (8)$$

where G is the shear modulus, and b is the Burgers vectors. For FCC crystals, $b^2 = 0.5a^2$. The larger the dislocation strain energy, the lower the plastic deformation ability and the higher the tensile strength. The dislocation strain energy of Cu-Sn and Cu-Sn-X is shown in Figure 3f. Doping of Ag, Ni, and Zr atoms leads to an increase in dislocation energy, while doping of Ca, Cd, and Mg atoms results in a decrease in dislocation energy. The variation trend of dislocation energy is consistent with the variation trend of shear modulus, which can be explained by motion theory.

In general, polycrystalline materials do not exhibit isotropic elastic properties, which means they display direction-dependent anisotropic properties. The mechanical response of materials to external stresses is typically controlled by the elastic anisotropy factor. Therefore, the study and description of this factor are crucial for material manufacturing. The Universal anisotropy factor of Cu-Sn and the Cu-Sn alloy can be examined through the subsequent Equation [28].

$$A^U = 5 \frac{G_V}{G_R} + \frac{B_V}{B_R} - 6 \quad (9)$$

The parameter A^U takes into account the contributions of both the shear modulus and bulk modulus. The deviation of A^U from 0 indicates the degree of crystal anisotropy. The computational results are shown in Table 3. The doping of Cd and Ag atoms into the Cu-Sn alloy leads to an increase in A^U , while the doping of Ag, Ca, Ni, and Zr results in a decrease in A^U .

Table 3. Cu-Sn alloy and Cu-Sn-X alloy mechanical properties.

Structure	B (GPa)	G (GPa)	E (GPa)	B/G	ν	W/J·m ^{−1}	A^U
Cu-Sn	188.518	44.192	122.967	4.266	0.391	1.155	5.013
Cu-Sn-Ag	131.800	60.624	157.694	2.174	0.301	1.645	0.498
Cu-Sn-Ca	120.637	38.438	104.243	3.138	0.356	1.068	2.722
Cu-Sn-Cd	125.964	35.024	96.160	3.597	0.372	0.956	7.799
Cu-Sn-Mg	122.344	36.208	98.870	3.379	0.365	0.981	6.978
Cu-Sn-Ni	134.054	63.085	163.593	2.125	0.297	1.689	0.899
Cu-Sn-Zr	129.903	44.928	120.852	2.891	0.345	1.241	1.840

In order to see the variation in the Young's modulus, we have examined the 3D plots of Cu-Sn and Cu-Sn-X through the Elastic POST [30]. The Cu-Sn and Cu-Sn-X alloys investigated in this study belong to the cubic crystal system, and the directional dependence of their Young's modulus can be obtained from the calculated compliance constants, which can be expressed as [27]

$$\frac{1}{E} = S_{11} - (2S_{11} - 2S_{12} - S_{44}) \left(l_1^2 l_2^2 + l_2^2 l_3^2 + l_3^2 l_1^2 \right) \quad (10)$$

E represents the Young's modulus, S_{ij} denotes the elastic flexibility coefficient, and l_1 , l_2 , and l_3 are the directional cosines.

Figure 4 illustrates the three-dimensional projection map of the Young's modulus anisotropy. The square represents the isotropy of the material, while any deviation from a perfect square represents the anisotropy of the material. The outer surface of the square has a higher Young's modulus, while the interior has a lower Young's modulus.

3.3. Electronic Structure Properties

The stability and mechanical properties of materials depend on their electronic structures. In order to further analyze the electronic structure of Cu-Sn-X (X = Ag, Ca, Cd, Mg, Ni, Zr) alloys from a microscopic perspective, the electronic density of states, occupation numbers, and differential charge densities were calculated for Cu-Sn alloys and Cu-Sn-X alloys. To analyze the bonding properties of Cu-Sn alloys and Cu-Sn-X alloys, the electronic density of states was examined. Figure 5 shows the total and partial electronic density of states for Cu-Sn alloys and Cu-Sn-X alloys, with the Fermi level represented by dashed lines. It can be observed that both Cu-Sn alloys and Cu-Sn-X alloys exhibit significant electron densities around the Fermi level, indicating typical metallic characteristics. Known to all, the pseudogap is defined as the valley of the Fermi level (E_f), where there are two peaks in the density of states (DOS) on each side of a nonzero Fermi level. The presence of the pseudogap indicates the existence of covalent bonds.

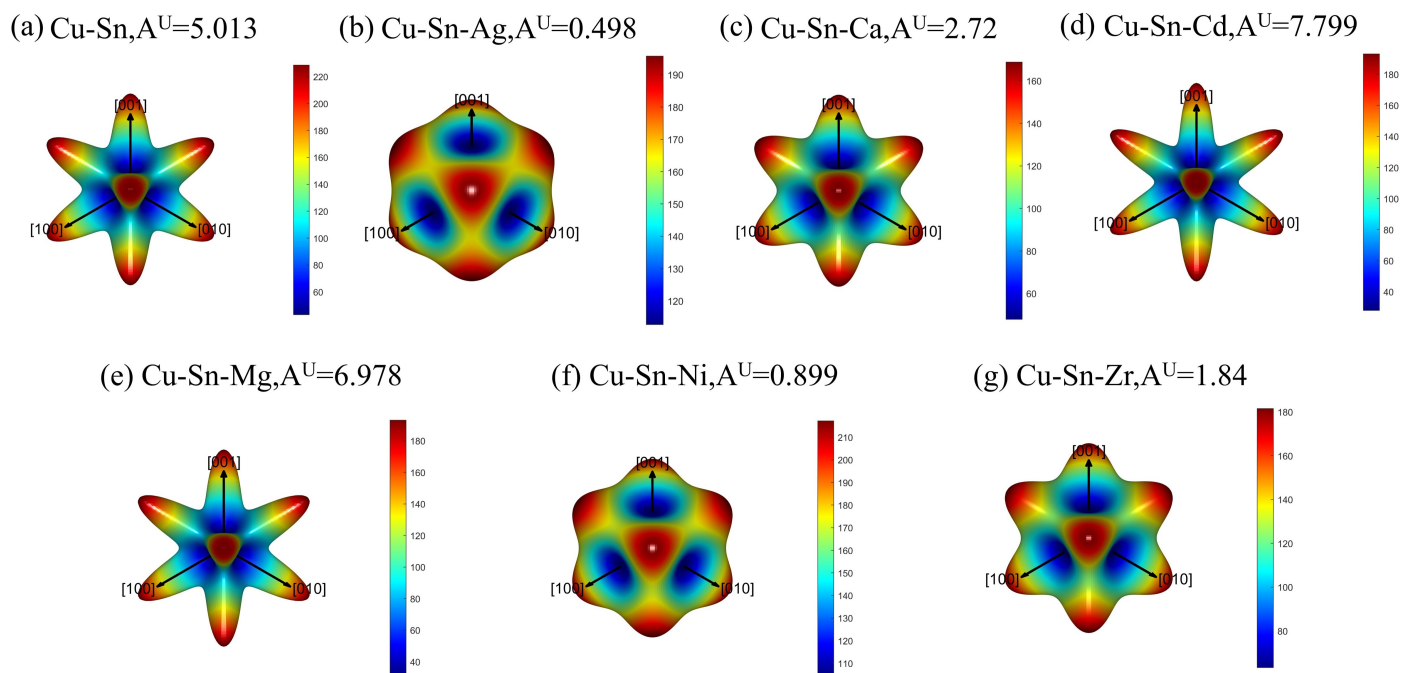


Figure 4. Three-dimensional surfaces of the Young's modulus for Cu-Sn and Cu-Sn-X alloys: (a) Cu-Sn, (b) Cu-Sn-Ag, (c) Cu-Sn-Ca, (d) Cu-Sn-Cd, (e) Cu-Sn-Mg, (f) Cu-Sn-Ni, (g) Cu-Sn-Zr.

As shown in Figure 5a, the total density of states in Cu-Sn alloys is primarily contributed by the d orbitals of Cu, with a sharp peak in the energy range of -10.17 eV to -9.14 eV mainly originating from the s orbitals of Sn. Figure 5b demonstrates that when Ag is doped into the Cu-Sn alloy to form Cu-Sn-Ag alloy, there is a sharp peak in the energy range of -7.12 eV to -4.18 eV, mainly contributed by the d orbitals of Ag. In Figure 5c, the overall density of states for the Cu-Sn-Ca alloy after Ca doping reveals two sharp peaks in the energy ranges of -42.07 eV to 39.56 eV and -21.88 eV to 20.68 eV, corresponding to the contributions from the s and p orbitals of Ca, respectively. After Cd doping, as illustrated in Figure 5d, a sharp peak arises in the energy range of -9.93 eV to -8.63 eV due to the d orbital contributions of Cd. Figure 5e shows that after Mg doping, a sharp peak is observed in the energy range of -42.77 eV to -41.36 eV, contributed by the p orbitals of Mg. In the case of Ni doping, no sharp peak is observed in the total density of states. After Zr doping, sharp peaks emerge in the energy ranges of -50.95 eV to -48.54 eV and -27.62 eV to -26.53 eV, corresponding to the contributions from the s and p orbitals of Zr, respectively.

In order to further characterize the strength of chemical bonds, bond lengths and Mulliken's bond populations were calculated. Mulliken's bond populations also confirm the presence of covalent bonds in Cu-Sn and Cu-Sn-X alloys. Positive bond populations indicate bonding states between two atoms, while negative bond populations represent anti-bonding states. In general, larger positive bond populations correspond to stronger bonding strength. Figure 6 illustrates that the Cu-Cu bond has a shorter bond length and a larger population value, indicating stronger bonding strength. When X (X = Ag, Ca, Cd, Mg, Ni, Zr) atoms are doped into the Cu-Sn alloy, X atoms are more likely to form bonds with Cu. As depicted in Figure 6c,f,g, when only Ca, Ni, and Zr atoms are doped, they can bond with Sn to form Ca-Sn, Ni-Sn, and Zr-Sn bonds, but these three bonds have smaller population value. The analogous relationship between the covalent bond strength and phase stability of Cu-Sn and Cu-Sn-X alloys can be obtained through bond groups. Therefore, when Ca, Cd, and Mg atoms are doped into Cu-Sn alloys, it is found that the Mulliken's bond populations are relatively small, resulting in weaker covalent bonds. This is consistent with the calculated cohesive energy results.

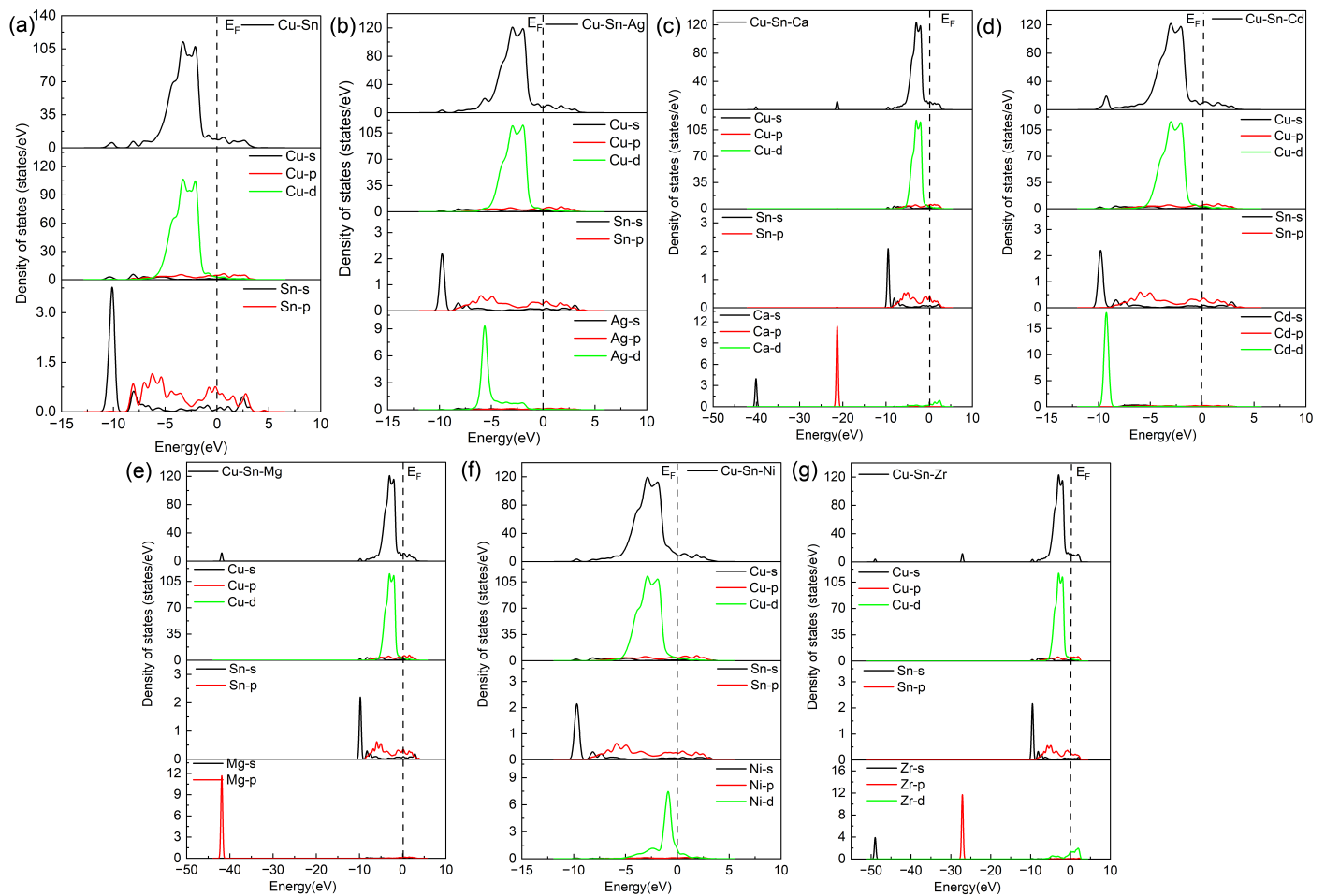


Figure 5. Total and partial electronic densities of states of Cu-Sn and Cu-Sn-X: (a) Cu-Sn, (b) Cu-Sn-Ag, (c) Cu-Sn-Ca, (d) Cu-Sn-Cd, (e) Cu-Sn-Mg, (f) Cu-Sn-Ni, (g) Cu-Sn-Zr.

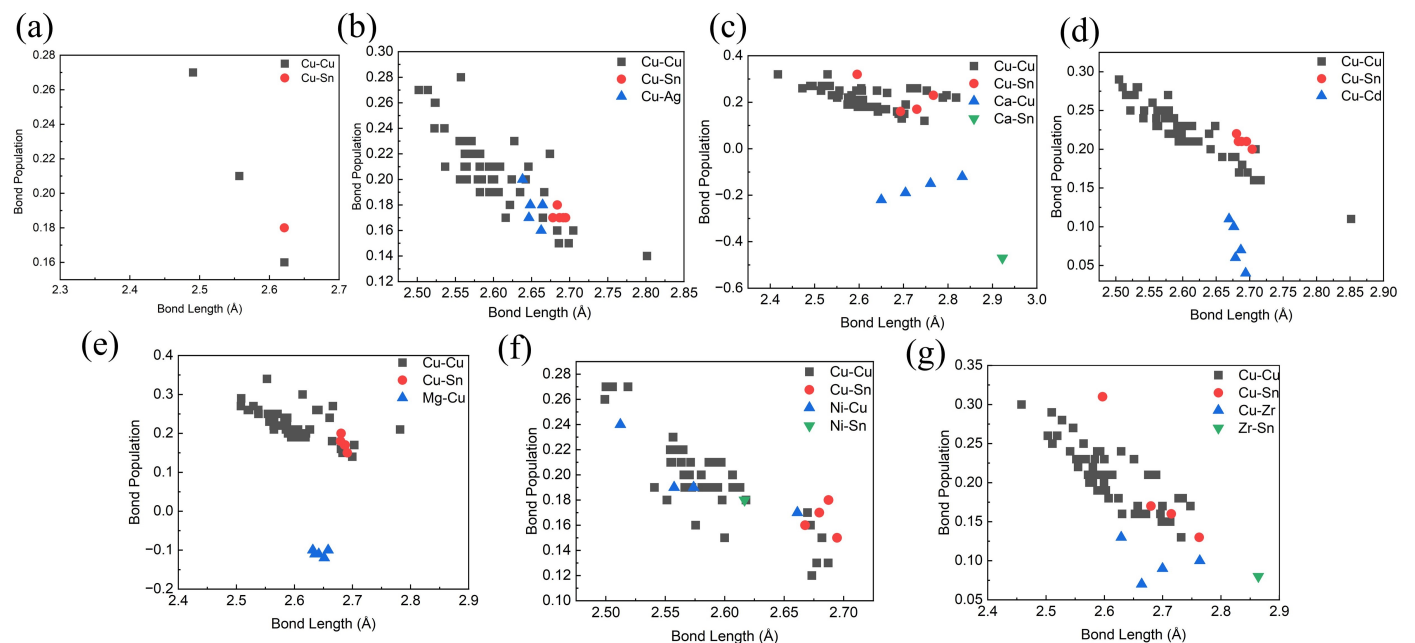


Figure 6. Cu-Sn alloy and Cu-Sn-X alloy bond length and occupation numbers. (a) Cu-Sn, (b) Cu-Sn-Ag, (c) Cu-Sn-Ca, (d) Cu-Sn-Cd, (e) Cu-Sn-Mg, (f) Cu-Sn-Ni, (g) Cu-Sn-Zr.

To gain further insight into electron transfer, the distribution of differential electron density on the (111) surface of Cu-Sn alloy and Cu-Sn-X alloys was investigated. As depicted in Figure 7, gained electrons are represented by blue regions, while lost electrons are indicated by red regions. The variation in charge density around the Cu atom signifies metallic bonding in pure Cu, while the petal-shaped charge density around the Sn atom indicates the formation of a covalent bond with Cu. Figure 7a suggests that Cu atoms tend to lose electrons, while Sn atoms tend to gain electrons. However, with the introduction of X (X = Ag, Ca, Cd, Mg, Ni, Zr) atoms into the Cu-Sn alloy, X atoms are capable of gaining electrons, indicating a substantial electron participation in chemical bonding between X and Cu atoms, resulting in the formation of stable bonding strength.

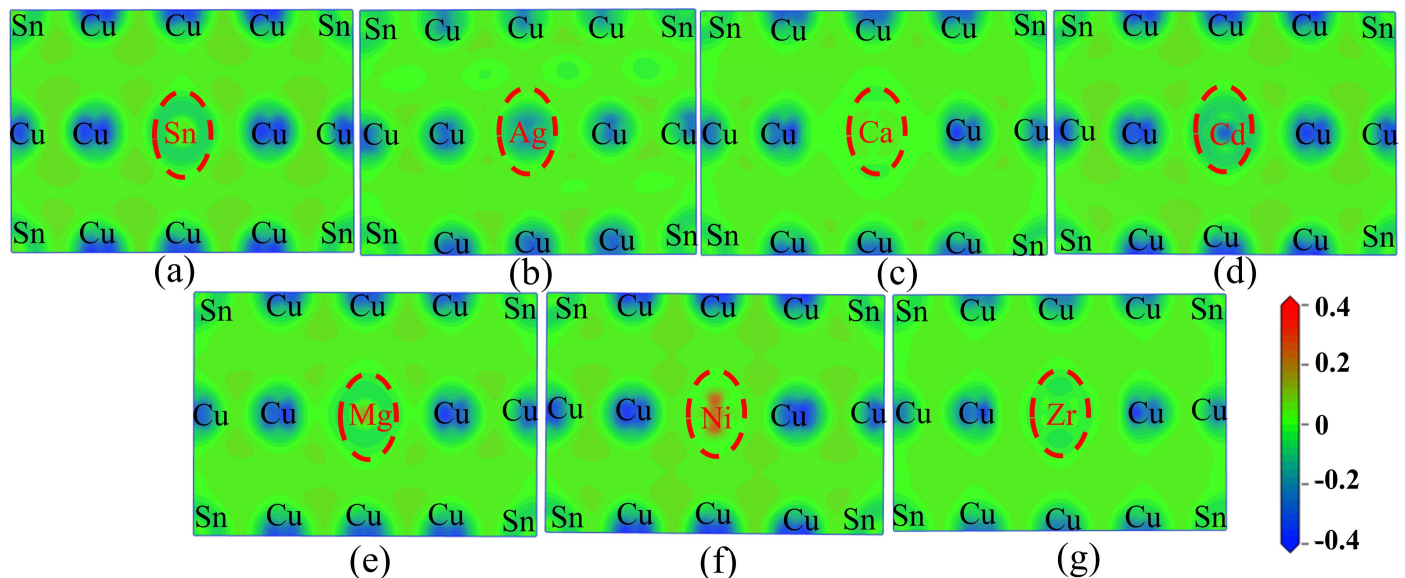


Figure 7. Electron density difference distribution cloud maps of Cu-Sn alloy and Cu-Sn-X alloy on the (111) surface. (a) Cu-Sn, (b) Cu-Sn-Ag, (c) Cu-Sn-Ca, (d) Cu-Sn-Cd, (e) Cu-Sn-Mg, (f) Cu-Sn-Ni, (g) Cu-Sn-Zr.

4. Conclusions

In this study, first-principles method was used to investigate the Cu-Sn-X (X = Ag, Ca, Cd, Mg, Ni, Zr) alloys formed by the addition of X atoms to Cu-Sn. The geometrical structures of Cu-Sn and Cu-Sn-X were optimized, and various properties including thermodynamic stability, mechanical properties, and electronic structures were calculated. The following conclusions were obtained:

(1) The calculation results of the cohesive energy for Cu-Sn-X structures after X (X = Ag, Ca, Cd, Mg, Ni, Zr) atom doping indicate that these Cu-Sn-X structures can stably exist, with the most stable structure being Cu-Sn-Ni. The cohesive energy value of Cu-Sn-Ni structure is -3.84 eV.

(2) The calculation results of mechanical properties show that doping of X atoms (X = Ag, Ca, Cd, Mg, Ni, Zr) leads to a decrease in the bulk modulus, Poisson's ratio, and B/G ratio. However, doping Ag and Ni atom can improve shear modulus, Young's modulus, and strain energy of the dislocation. The doping of Ni has the highest enhancement on the shear modulus, Young's modulus, and strain energy of the dislocation, with respective values as follows: 63.085 GPa, 163.593 GPa, and 1.689 W/J·m $^{-1}$.

(3) An analysis of the electronic structure of Cu-Sn-X alloys with X (X = Ag, Ca, Cd, Mg, Ni, Zr) doping reveals that the performance differences in Cu-Sn-X alloys originate from the Mulliken's bond populations of Cu-X. The doping of Ni and Ag atoms holds promise for achieving Cu-Sn alloys with superior overall performance.

Author Contributions: Conceptualization, Z.W. and J.C.; data curation, Z.W., J.C. and N.Q.; formal analysis, Y.X.; funding acquisition, Y.L., J.Z. and H.T.; investigation, Y.L.; methodology, N.Q.;

resources, Y.X. and B.W.; software, J.X.; supervision, Y.L.; validation, N.Q.; visualization, L.S., Y.X. and B.W.; writing—original draft, Z.W.; writing—review & editing Y.L., L.S., J.Z. and H.T. All authors have read and agreed to the published version of the manuscript.

Funding: This research received no external funding.

Data Availability Statement: The raw data supporting the conclusions of this article will be made available by the authors on request.

Conflicts of Interest: Author Ling Sun, Yuchen Xiao, Baoan Wu, Huiyi Tang were employed by the company China Steel Corporation. The remaining authors declare that the research was conducted in the absence of any commercial or financial relationships that could be construed as a potential conflict of interest.

References

1. Kuang, G.; Miao, K.; Li, X.; Wu, H.; Liu, C.; Li, R.; Fan, G. In-situ observation of microstructure and orientation evolution of the Cu–Cr–Zr–Hf alloys. *Mater. Sci. Eng. A* **2023**, *865*, 144642. [\[CrossRef\]](#)
2. Jiabin, L.; Menglian, H.; Huiya, Y.; Hongbin, X.; Chao, Y.; Jindong, Z.; Qiong, F.; Litian, W.; Liang, M.; Hongtao, W. In-situ TEM study of the dynamic interactions between dislocations and precipitates in a Cu–Cr–Zr alloy. *J. Alloys Compd.* **2018**, *765*, 560–568.
3. Wang, Y.D.; Wu, L.H.; Xue, P.; Zhang, H.; Ni, D.R.; Ma, Z.Y. Improved strength with good conductivity in Cu–Cr–Zr alloys: Determinant effect of under-aging treatment before rolling and aging. *Mater. Sci. Eng. A* **2022**, *848*, 143395. [\[CrossRef\]](#)
4. Lai, Z.; Mai, Y.; Song, H.; Mai, J.; Jie, X. Heterogeneous microstructure enables a synergy of strength, ductility and electrical conductivity in copper alloys. *J. Alloys Compd.* **2022**, *902*, 163646. [\[CrossRef\]](#)
5. Ma, B.; An, B.; Zhao, X.; Li, Y.; Du, J.; Wang, E. Microstructure and properties of Cu–Cr–Zr alloy by doping Sc. *Mater. Lett.* **2023**, *336*, 133917. [\[CrossRef\]](#)
6. Liu, Y.; Zhou, Y.; Lu, C.; Gan, K.; Du, Y.; Liu, A.; Meng, F.; Liu, G.; Gong, Y.; Song, K.; et al. Nano-precipitates evolution and properties improvement mechanism of Cu–Zn–Ni–Si–X alloy strip based on multi-element microalloying and thermomechanical treatment. *J. Mater. Res. Technol.* **2023**, *25*, 107–119. [\[CrossRef\]](#)
7. Li, L.; Kang, H.; Zhang, S.; Li, R.; Yang, X.; Chen, Z.; Guo, E.; Wang, T. Microstructure and properties of Cu–Cr–Zr (Mg) alloys subjected to cryorolling and aging treatment. *J. Alloys Compd.* **2023**, *938*, 168656. [\[CrossRef\]](#)
8. Huang, L.; Cui, Z.; Meng, X.; Li, X.; Sheng, X.; Lei, Q. Effect of trace alloying elements on the stress relaxation properties of high strength Cu–Ti alloys. *Mater. Sci. Eng. A* **2022**, *846*, 143281. [\[CrossRef\]](#)
9. Lei, Q.; Xiao, Z.; Hu, W.; Derby, B.; Li, Z. Phase transformation behaviors and properties of a high strength Cu–Ni–Si alloy. *Mater. Sci. Eng. A* **2017**, *697*, 37–47. [\[CrossRef\]](#)
10. Yang, J.; Ouyang, P.; Liu, T.; Yun, H.; Sun, W.; Wang, Y.; Liu, J.; Zhang, S. First-principles study of the effect of aluminum content on the elastic properties of Cu–Al alloys. *Mater. Today Commun.* **2022**, *31*, 103399. [\[CrossRef\]](#)
11. Yang, Q.; Yin, D.Q.; Ge, J.Q.; Chen, J.; Wang, S.L.; Peng, H.B.; Wen, Y.H. Suppressing heating rate-dependent martensitic stabilization in ductile Cu–Al–Mn shape memory alloys by Ni addition: An experimental and first-principles study. *Mater. Charact.* **2018**, *145*, 381–388. [\[CrossRef\]](#)
12. He, D.; Liu, G.; Liu, J.; Xie, H.; Yue, D.; Chen, Z.; Wei, C.; Xu, X.; Xie, H. Study of effects of corrosion temperature on corrosion resistance of Cu–C alloys to liquid Ga. *Corros. Sci.* **2023**, *211*, 110917. [\[CrossRef\]](#)
13. Dong, H.; Zhong, R.; Liu, L.; Wang, Z.; Yang, C.; Luo, Z.; Zhang, W. The intergranular precipitation behavior of G phase in a high-performance complex cast Cu–Ni–Al alloy. *Mater. Charact.* **2023**, *196*, 112611. [\[CrossRef\]](#)
14. Iwaoka, H.; Hirose, S. First-principles calculation of elastic properties of Cu–Zn intermetallic compounds for improving the stiffness of aluminum alloys. *Comput. Mater. Sci.* **2020**, *174*, 109479. [\[CrossRef\]](#)
15. Liu, Y.; Wang, L.; Jiang, K.; Yang, S. Electro-deposition preparation of self-standing Cu–Sn alloy anode electrode for lithium ion battery. *J. Alloys Compd.* **2019**, *775*, 818–825. [\[CrossRef\]](#)
16. Singh, J.B.; Cai, W.; Bellon, P. Dry sliding of Cu–15 wt%Ni–8 wt%Sn bronze: Wear behaviour and microstructures. *Wear* **2007**, *263*, 830–841. [\[CrossRef\]](#)
17. Davis, J.R. *ASM Specialty Handbook: Copper and Copper Alloys*; ASM International: Detroit, MI, USA, 2001.
18. Yang, P.; He, D.; Shao, W.; Tan, Z.; Guo, X.; Lu, S.; Anton, K. Study of the microstructure and mechanical properties of Cu–Sn alloys formed by selective laser melting with different Sn contents. *J. Mater. Res. Technol.* **2023**, *24*, 5476–5485. [\[CrossRef\]](#)
19. Zhang, L.; Li, Y.; Zhou, R.; Wang, X.; Wang, Q.; Xie, L.; Li, Z.; Xu, B. First-Principles Study of the Effect of Sn Content on the Structural, Elastic, and Electronic Properties of Cu–Sn Alloys. *Crystals* **2023**, *13*, 1532. [\[CrossRef\]](#)
20. Segall, M.D.; Lindan, P.J.D.; Probert, M.J.; Pickard, C.J.; Hasnip, P.J.; Clark, S.J.; Payne, M.C. First-principles simulation: Ideas, illustrations and the CASTEP code. *J. Phys. Condens. Matter* **2002**, *14*, 2717. [\[CrossRef\]](#)
21. Huang, J.; Xue, J.; Li, M.; Cheng, Y.; Lai, Z.; Hu, J.; Zhou, F.; Qu, N.; Liu, Y.; Zhu, J. First-Principles Computation of Microscopic Mechanical Properties and Atomic Migration Behavior for Al4Si Aluminum Alloy. *Metals* **2023**, *13*, 1622. [\[CrossRef\]](#)
22. Djemia, P.; Benhamida, M.; Bouamama, K.; Belliard, L.; Faurie, D.; Abadías, G. Structural and elastic properties of ternary metal nitrides $Ti_xTa_{1-x}N$ alloys: First-principles calculations versus experiments. *Surf. Coat. Technol.* **2013**, *215*, 199–208. [\[CrossRef\]](#)

23. Uesugi, T.; Higashi, K. First-principles studies on lattice constants and local lattice distortions in solid solution aluminum alloys. *Comput. Mater. Sci.* **2013**, *67*, 1–10. [[CrossRef](#)]
24. Chong, X.; Jiang, Y.; Zhou, R.; Feng, J. Elastic properties and electronic structures of CrxBy as superhard compounds. *J. Alloys Compd.* **2014**, *610*, 684–694. [[CrossRef](#)]
25. Zhang, X.; Wang, D.; Zhou, Y.; Chong, X.; Li, X.; Zhang, H.; Nagaumi, H. Exploring crystal structures, stability and mechanical properties of Fe, Mn-containing intermetallics in Al-Si Alloy by experiments and first-principles calculations. *J. Alloys Compd.* **2021**, *876*, 160022. [[CrossRef](#)]
26. Ranganathan, S.I.; Ostoja-Starzewski, M. Universal Elastic Anisotropy Index. *Phys. Rev. Lett.* **2008**, *101*, 055504. [[CrossRef](#)] [[PubMed](#)]
27. Browaeys, J.T.; Chevrot, S. Decomposition of the elastic tensor and geophysical applications. *Geophys. J. Int.* **2004**, *159*, 667–678. [[CrossRef](#)]
28. Moakher, M.; Norris, A.N. The Closest Elastic Tensor of Arbitrary Symmetry to an Elasticity Tensor of Lower Symmetry. *J. Elast.* **2006**, *85*, 215–263. [[CrossRef](#)]
29. Wang, G.; Jiang, Y.; Li, Z.; Chong, X.; Feng, J. Balance between strength and ductility of dilute Fe2B by high-throughput first-principles calculations. *Ceram. Int.* **2021**, *47*, 4758–4768. [[CrossRef](#)]
30. Liao, M.; Liu, Y.; Min, L.; Lai, Z.; Han, T.; Yang, D.; Zhu, J. Alloying effect on phase stability, elastic and thermodynamic properties of Nb-Ti-V-Zr high entropy alloy. *Intermetallics* **2018**, *101*, 152–164. [[CrossRef](#)]

Disclaimer/Publisher’s Note: The statements, opinions and data contained in all publications are solely those of the individual author(s) and contributor(s) and not of MDPI and/or the editor(s). MDPI and/or the editor(s) disclaim responsibility for any injury to people or property resulting from any ideas, methods, instructions or products referred to in the content.